Clays and Clay Minerals, Vol. 43, No. 2, 159–173, 1995.

PERIODIC AND NONPERIODIC STACKING IN BIOTITE FROM THE BINGHAM CANYON PORPHYRY COPPER DEPOSIT, UTAH

HUIFANG XU* AND DAVID R. VEBLEN

Department of Earth and Planetary Sciences, The Johns Hopkins University, Baltimore, Maryland 21218

Abstract—Fine-grained biotite crystals within primary actinolite from a quartz monzonite body of the Bingham Canyon porphyry copper deposit, Utah, consist of 1M, $5M_1$, and $1M_d$ polytype structures. HRTEM images directly show the stacking sequences of ordered biotite polytypes, stacking faults in ordered polytypes, and stacking sequences in disordered polytypes, if the stacking vectors for the 2:1 layers involve only 0° and ±120° rotations. The most common type of stacking fault in the 1M biotite is a layer with −120° rotation, followed by a layer with +120° rotation, which corresponds to one unit cell of the $2M_1$ polytype inserted in the 1M structure. Disordered (or semi-random) biotite is composed primarily of thin domains of the 1M and $2M_1$ polytypes, with stacking faults. The structure of a new 5-layer ($5M_1$) polytype has been determined from SAED and HRTEM results. The stacking sequence of the polytype is [02022].

A model of structural oscillation among 1M, $2M_1$, and 3T structural states is proposed to interpret nonperiodic stacking sequences in biotite crystals formed during non-equilibrium crystallization. The model also provides qualitative insights into the structure of complex long-period polytypes and may help to explain intergrowths of ordered and disordered polytypes that form during crystallization far from the equilibrium state.

Key Words—5-Layer mica polytypes, Biotite, Transmission electron microscopy, Structural oscillation.

INTRODUCTION

Polytypism in the biotite mica is a well-known phenomenon (e.g., Bailey 1988, Baronnet 1992, Ross *et al* 1966, Smith and Yoder 1956), and multiple-polytype assemblages can form in a wide range of geological settings. Because the pseudohexagonal 2:1 layers in Mg-Fe trioctahedral micas are ditrigonally distorted, virtually all observed stacking sequences involve layer rotations of 0° and ±120° (Ross *et al* 1966). Therefore, it is possible to determine the stacking sequences directly from high-resolution transmission electron microscopy (HRTEM) images (Iijima and Buseck 1978) and to derive the polytype structures for biotite with an ordered stacking sequence. Assuming that the mica polytypes involve only 0° and ±120° rotations, polytype-sensitive diffraction information appears in *hkl* ($k \neq 3n$) diffraction rows (Ross *et al* 1966).

It is also common to find biotite crystals with syntactic coalescence of several ordered polytypes and disordered polytypes. Different polytypes (ordered and disordered) in a single crystal with syntactic texture may show compositional differences (Baronnet and Kang 1989), or they may show no compositional difference (Takeda and Ross 1975). The detailed X-ray diffraction study of Takeda and Ross (1975) further shows that coexisting 1M and $2M_1$ biotite crystals formed under the same conditions and with the same composition can exhibit subtle differences in the structures of their 2:1 layers.

Although both equilibrium and kinetic theories (most related to screw dislocations and spiral growth) can be used to interpret ordered polytypes with both short and long periods (Baronnet 1992), as well as the intergrowth of different polytypes (Vand and Hanoka 1967), there is no quantitative theory to explain the details of disordered (or nonperiodic) stacking sequences and some types of intergrowth that are observed between ordered and disordered polytype domains that formed in micas during crystal growth. In this paper, we apply HRTEM and selected-area electron diffraction (SAED) to identify ordered polytypes (e.g., a 5-layer polytype), stacking faults within ordered polytypes, and the stacking sequences and intergrowth of different polytype domains in semi-random polytypes. A crystallization mechanism is also proposed for disordered polytypes and the intergrowth of different polytype domains formed during crystallization far from equilibrium state. This mechanism may provide a heuristic basis for understanding the formation of some disordered mica polytypes and intergrowths.

HRTEM SIMULATIONS

Simulated HRTEM images and electron diffraction patterns were calculated using a demonstration version of the MACTEMPAS computer program kindly provided by Dr. M. A. O'Keefe. The input structure was based on the 1M phlogopite structure refinement from

* Present address: Department of Geology, Arizona State University, Tempe, Arizona 85287, Phone: (602) 965-7250, FAX: (602) 965-8102.

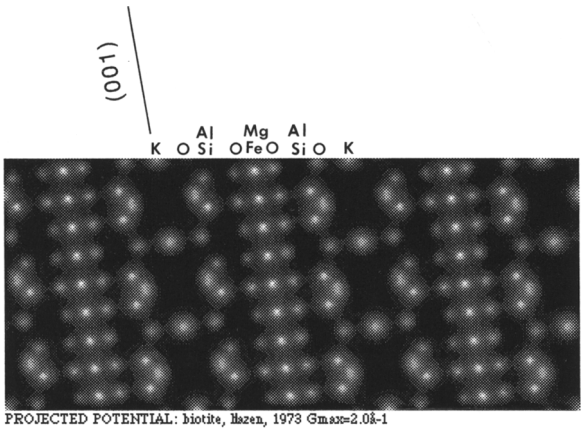

Figure 1. Electron potential of 1M biotite projected onto the [110]*-c* plane. The white dots correspond to K, O, (Al,Si), and (Mg,Fe) atoms, respectively.

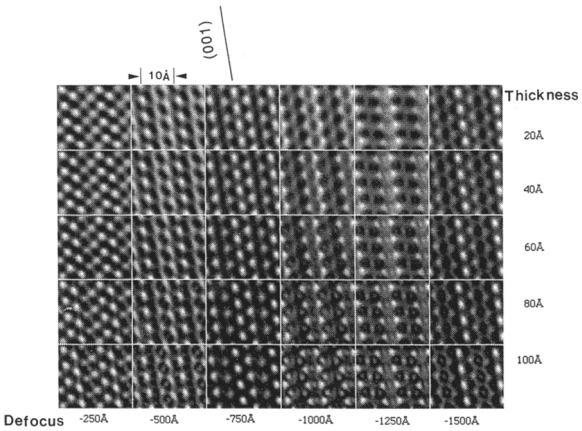

Figure 2. Calculated HRTEM images of 1M biotite with different thicknesses and at different defocus conditions.

Hazen and Burnham (1973), and the biotite structural formula for the simulations was based on analytical electron microscopy (AEM) analyses of 1M biotite from our specimen (Table 1). The interlayer position was assumed to be filled by K atoms. Al was assumed to be randomly distributed in the tetrahedral sites, and Fe and Mg was assumed to be randomly in the octahedral sites (M_1 and M_2), in ratio of 1:2.

Optical parameters for a Philips 420ST transmission electron microscope were used (spherical aberration coefficient C_s = 1.2 mm; accelerating voltage = 120 keV, etc.). Different specimen thicknesses (ranging from 4 to 20 unit cells parallel to the [1$\bar{1}$0] direction, i.e., from approximately 20 Å to 100 Å) and defocus values (ranging from −250 Å to −1500 Å) were used. Figure 1 shows electron potential of the model biotite projected onto the [110]*−c* plane. The white spots correspond to the projected atomic positions of the structure.

Figure 2 illustrates calculated HRTEM images of the 1M biotite at different thicknesses and defocus conditions. It can be seen that the calculated HRTEM images are sensitive to defocus, but not so sensitive to the calculated range of specimen thickness. This result is in agreement with those for a 1M phlogopite structure calculated by Amouric *et al* (1981). The calculated HRTEM images at defocus values of −750 Å and −1500 Å are very similar. Bright areas in the calculated HRTEM images at these defocus values correspond to areas of low electron density, especially for the interlayer regions. Because the 2:1 layer (i.e., the fundamental TOT layer unit that is stacked to form polytypes) for polytypes are almost identical in structure and chemical composition (Verma and Krishna 1966, Bailey *et al* 1977), and due to the pseudohexagonal symmetry of mica layers, stacking faults in ordered mica polytypes can be identified easily based on relative shifts of the neighboring unit layers on HRTEM images. It is also possible to identify complex multiple-layer mica polytypes involving 0° and ±120° rotations from images obtained in certain orientations, based on the relative shifts of neighboring 2:1 layers with respect to a reference layer (Iijima and Buseck 1978, Baronnet and Kang 1989, Baronnet 1992).

Figure 3 illustrates a calculated electron diffraction pattern from a perfectly oriented biotite crystal with uniform 100 Å thickness. It can be seen that the intensities of some hkl diffractions are not equal to the corresponding intensities of $\overline{hkl}$ diffractions, for ex-

Table 1. Structural formulae of 1M, $1M_d$, $5M_1$ biotite crystals.

	Structural formula
1M biotite	$(K_{0.79},Na_{0.02},Ca_{0.08})_{0.89}(Mg_{1.63},Fe_{1.02},Al_{0.08},Mn_{0.01},Ti_{0.14})_{2.88}[(Si_{2.92},Al_{1.09})_4O_{10}](OH)_2$
1M biotite	$(K_{0.81},Na_{0.16},Ca_{0.08})_{1.05}(Mg_{1.73},Fe_{1.00},Mn_{0.01},Ti_{0.10})_{2.84}[(Si_{2.84},Al_{1.12},Ti_{0.04})_4O_{10}](OH)_2$
1M biotite	$(K_{0.85},Na_{0.20},Ca_{0.04})_{1.09}(Mg_{1.82},Fe_{0.95},Mn_{0.01},Ti_{0.11})_{2.89}[(Si_{2.85},Al_{1.11},Ti_{0.04})_4O_{10}](OH)_2$
1M biotite	$(K_{0.81},Na_{0.16},Ca_{0.02})_{0.99}(Mg_{1.73},Fe_{0.99},Mn_{0.01},Ti_{0.16})_{2.89}[(Si_{2.84},Al_{1.13},Ti_{0.03})_4O_{10}](OH)_2$
$5M_1$ biotite	$(K_{0.80},Ca_{0.02})_{0.82}(Mg_{1.86},Fe_{0.91},Ti_{0.18})_{2.95}[(Si_{2.84},Al_{1.12},Ti_{0.04})_4O_{10}](OH)_2$
$5M_1$ biotite	$(K_{0.72},Ca_{0.02})_{0.72}(Mg_{1.80},Fe_{0.92},Ti_{0.22})_{2.94}[(Si_{2.88},Al_{1.08},Ti_{0.04})_4O_{10}](OH)_2$
$5M_1$ biotite	$(K_{0.71},Na_{0.01})Ca_{0.01})_{0.73}(Mg_{1.81},Fe_{0.89},Ti_{0.21})_{2.94}[(Si_{2.87},Al_{1.12},Ti_{0.01})_4O_{10}](OH)_2$
$1M_d$ biotite	$(K_{0.69},Na_{0.23},Ca_{0.07})_{0.99}(Mg_{2.11},Fe_{0.74},Ti_{0.03},Al_{0.02},Mn_{0.01})_{2.85}[(Si_{3.01},Al_{0.99})_4O_{10}](OH)_2$
$1M_d$ biotite	$(K_{0.69},Na_{0.18},Ca_{0.03})_{0.90}(Mg_{2.30},Fe_{0.76},Mn_{0.01})_{2.94}[(Si_{3.03})Al_{0.93})_{3.96}O_{10}](OH)_2$

https://doi.org/10.1346/CCMN.1995.0430203 Published online by Cambridge University Press

ample, 002 and 00$\bar{2}$; 11$\bar{5}$ and $\overline{11}5$; and 22$\bar{4}$ and $\overline{22}4$. Thus, Friedel's law is violated, due to complex dynamical interactions between the crystal and the electron beam. This underscores the fact that it is dangerous to infer the presence or absence of a center of symmetry, or to derive atomic coordinates, based on electron-diffraction intensity information (Gjonnes and Moodie 1965, Veblen 1985). For instance, the space group *Cm* might be wrongly assumed for a mica, based simply on unequal intensities of *hkl* and $\overline{hkl}$ diffraction spots. The present example shows that unequal intensities can alternatively arise for the centrosymmetric *C2/m* structure from dynamical diffraction effects. Suggestions that dioctahedral mica and mica-like minerals (sericite, illite, and smectite) are noncentrosymmetric based on electron diffraction intensities probably are not warranted due to the inherent poor quality of electron diffraction intensity data and the effects of dynamical diffraction illustrated by these calculations (Veblen 1981).

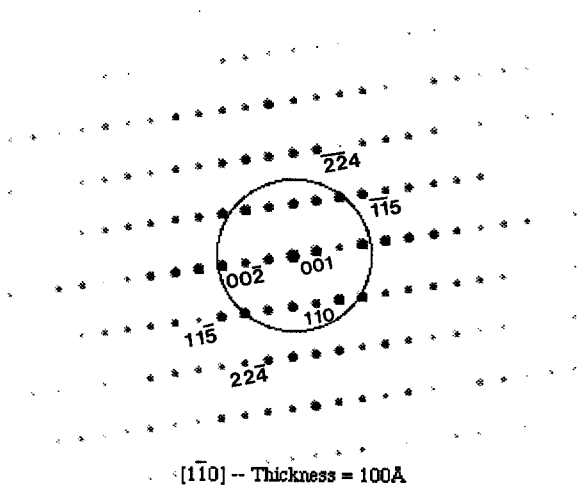

Figure 3. A calculated [1$\bar{1}$0] zone-axis electron diffraction pattern of 1M biotite in perfect orientation and with uniform 100-Å thickness. Intensities of the reflection pairs 002 and 00$\bar{2}$; 11$\bar{5}$ and $\overline{11}5$; and 22$\bar{4}$ and $\overline{22}4$ are not equal, due to complex dynamical interactions between the crystal and electron beam.

PETROGRAPHY OF THE SPECIMEN AND EXPERIMENTAL METHODS

The green biotite used in this study occurs as very fine platelets within actinolite crystals in a quartz monzonite specimen from the Bingham Canyon porphyry copper deposit, Utah (sample 659-3 of Bowman *et al* 1987). The actinolite crystals are weakly altered and occur either as rims around augite crystals or as isolated crystals, which were considered as a primary phase crystallized from magma (Bowman *et al* 1987). The quartz monzonite is genetically related to the Bingham Canyon porphyry ore deposit and shows hydrothermal alteration zones (potassic, propylitic, and argillic alterations) (Bowman *et al* 1987). The specimen is from the propylitic zone not far from the potassic alteration zone. Biotite and K-feldspar also occur as phenocrysts in the monzonite. The main alteration minerals are uralitic actinolite (i.e., replacing pyroxene), chlorite that commonly replaces the uralitic actinolite, epidote, quartz, calcite, and smectite that mainly replaces primary augite. Very weak argillic alteration also occurs in feldspars, and the smectite in augite also formed during late-stage argillic alteration. Isolated actinolite crystal was relatively stable during the propylitic and argillic stages of alteration, although there was minor alteration to smectite. Argillic alterations from feldspar to illite/smectite assemblage, and from augite and actinolite to smectite will be discussed in a separate paper. The fine biotite crystals have (001) almost parallel to (100) of the actinolite.

Actinolite crystals with biotite inclusions were selected for TEM investigation from petrographic thin sections so that their c-axes were nearly normal to the specimen surface. They were thinned by ion milling and coated with C. Because of the topotaxic relationship between the phyllosilicates and actinolite, these sections are also approximately normal to (001) of the included fine biotite and smectite. All transmission electron microscopy (TEM) and analytical electron microscopy (AEM) investigations were carried out with a Philips 420ST electron microscope equipped with an energy-dispersive X-ray detector and a Princeton Gamma-Tech analyzer as described by Veblen and Bish (1988) and Livi and Veblen (1987). Fe was assumed to be ferrous in reduction of all AEM analyses.

TEM RESULTS

1M biotite

Figure 4 shows [010] and [1$\bar{1}$0] zone-axis SAED patterns of a 1M biotite crystal within a primary actinolite. The SAED patterns were obtained from same area with different orientations. Structural formulae of the 1M biotite are listed in Table 1. Dynamical interaction between the crystal and the electron beam is quite obvious. For instance, the intensities of 001 and 002 reflections are similar (Figure 4) because of dynamical diffraction, even though structural factor of 002 reflection is much weaker than that of 001 reflection (Hazen and Burnham 1973). All diffraction spots are sharp, but there is very weak streaking in the 11*l* and 22*l* diffraction rows along the c^* direction (Figure 4b), probably caused by (001) stacking faults in the crystal. A HRTEM image corresponding to the [1$\bar{1}$0]-zone SAED pattern shows two areas with stacking faults (Figure 5). The image corresponds to the calculated HRTEM image at a defocus value of −750 Å. Under these conditions, the brightest white dots correspond

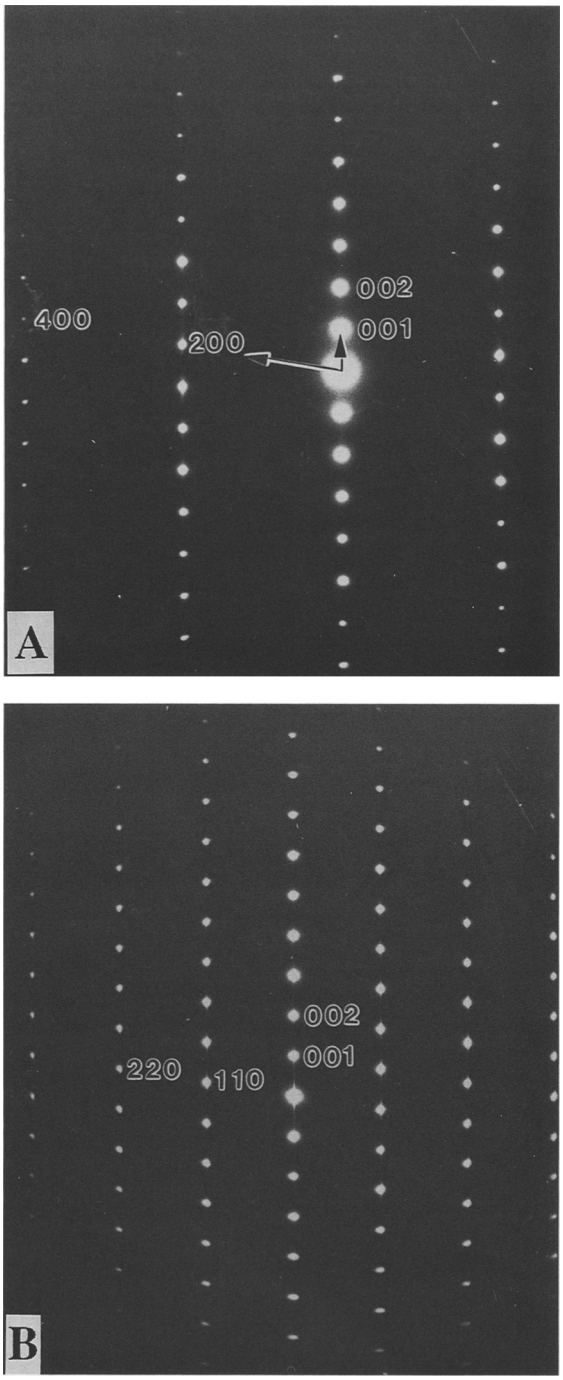

Figure 4. (a) A [010] zone-axis SAED pattern from 1M biotite. (b) A [1$\bar{1}$0] zone-axis SAED pattern of the biotite showing very weak streaking in hkl ($k \neq 3n$) diffraction rows caused by stacking faults.

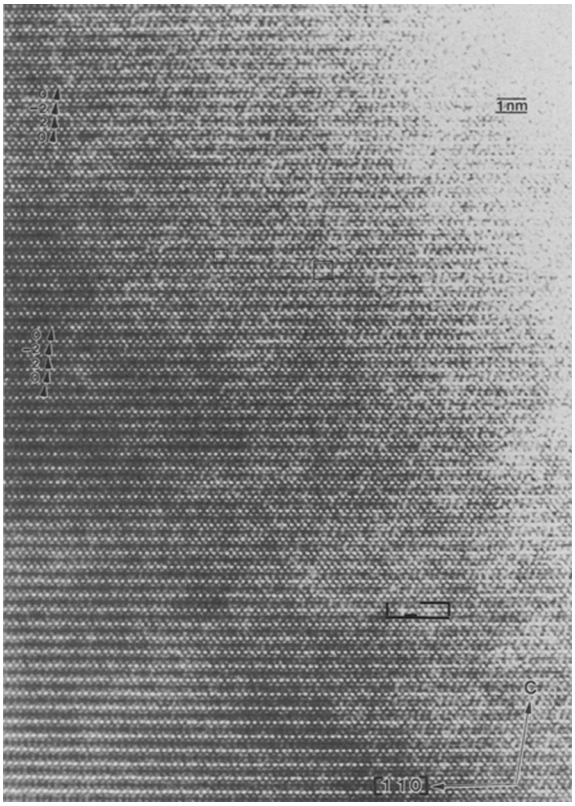

Figure 5. HRTEM image of 1M biotite showing two stacking faults. Each fault corresponds to insertion of one unit cell of the $2M_1$ polytype into the 1M structure. Some connected bright spots outlined by small blocks are probably caused by K-atom vacancies.

to the interlayer tunnels separated by K atoms, based on the HRTEM simulation (Figures 1 and 2) Some connected bright spots in the interlayer positions may be caused by K-atom vacancies (Figure 5). There is not much difference in the image from thin (upper-right corner) and relatively thick (lower-left corner) areas of the specimen. The 1M biotite domains that are separated by stacking faults keep the same orientation across the faults. The HRTEM image shows that each stacking fault corresponds to one unit cell of the $2M_1$ polytype, i.e., a layer with $-120°$ rotation followed by a layer with $+120°$ rotation. The image shifts between neighboring layers are the same as those in stacking-vector diagrams for the 1M and $2M_1$ polytypes (Figure 6). The "RTW" notation of Ross, Takeda, and Wones (1966) for mica polytypes and layer rotations is used to describe the rotations associated with the image shifts (Figure 5).

5M$_1$ biotite

A 5-layer biotite structure also was observed within the primary actinolite. The spots characterizing the 5-layer polytype in the 111 and 221 diffraction rows show a pronounced systematic variation of diffracted intensities: weak●strong●strong●strong●strong●weak . . . (Figure 7a). Indexing of the diffraction patterns in Fig-

https://doi.org/10.1346/CCMN.1995.0430203 Published online by Cambridge University Press

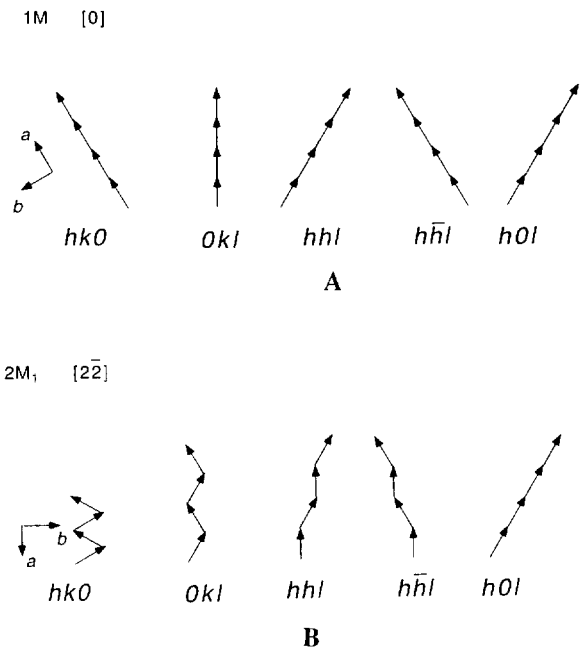

Figure 6. Diagrams showing stacking vectors in the 1M (A) and $2M_1$ (B) polytypes in different real-space sections.

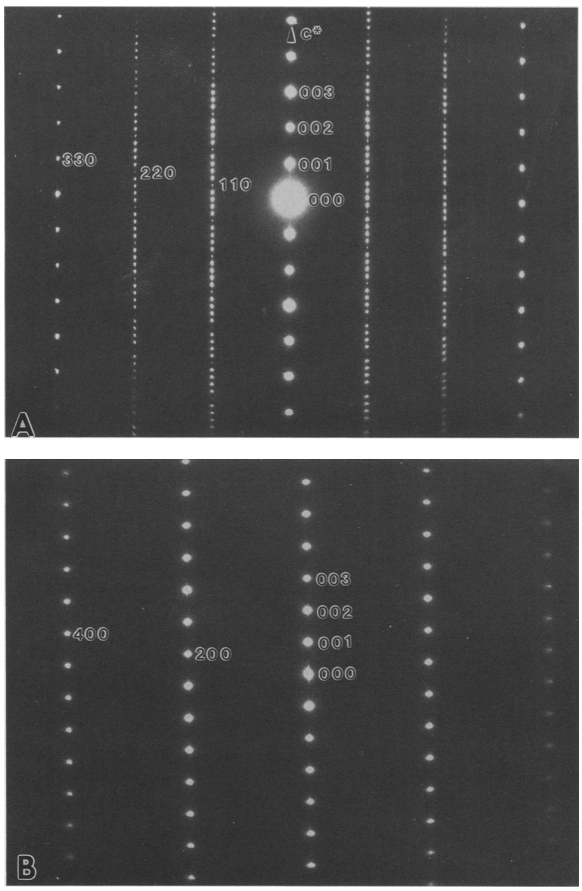

Figure 7. (a) A [1$\bar{1}$0] zone-axis SAED pattern from the 5-layer biotite polytype, showing additional diffraction spots characteristic of the 5-layer periodicity in the 11*l* and 22*l* diffraction rows. (b) A [010] zone-axis SAED pattern of the 5-layer biotite showing no additional diffraction spots.

ure 7 is based on the 1M mica axial setting. There are no additional diffraction spots characteristic of the 5-layer polytype in [010]-zone SEAD pattern (Figure 7b). Strong intensity of 002 reflection is caused by dynamical diffraction as that in 1M biotite. The intensity distribution in the 02*l* and 04*l* diffraction rows is similar to that in the 11*l* and 22*l* rows, and the intensities in the 13*l* rows is similar to that in the 00*l*, 20*l*, 40*l*, and 06*l* rows. Based on the observation that SAED patterns show additional diffraction spots only in *hkl* ($k \neq 3n$) rows, it can be inferred that this 5-layer biotite polytype involves only 0° and/or +120° rotations of the 2:1 layers (Ross *et al* 1966).

A dark-field image formed from the 110 diffraction spot and its nearby superstructure spots shows 50-Å periodicity along the c^* direction (Figure 8). An HRTEM image corresponding to calculated HRTEM images at a defocus value of −750 Å reveals the projected relative shifts of neighboring unit layers (Figure 9a). The image shows the shift sequence . . . |0,0,+,+,−|0,0,+,+,−| . . . , which is periodic and repeats every five layers. Based on the relative shifts, the relative rotations of the biotite layers with respect to reference layer at 0° are as follows: |0°, 0°, +120°, +120°, −120° (or +240°)|. The rotation angles relative to the neighboring layers are 120°, 0°, 120°, 0°, 120° . . . , and the corresponding stacking sequences represented in RTW notation are [20202] or [02022]. Figure 9b is a HRTEM image recorded at a defocus value of approximately −1250 Å (Figure 2), showing the same stacking sequence in the 5-layer biotite polytype, but with a stacking fault that results in one "unit cell" with only four unit layers (labeled "4"). The stacking sequences of the four layers are [0222], which is equivalent to a single unit cell of $4M_2$ mica (Ross *et al* 1966) and corresponds to the stacking of one 1M unit cell followed by one 3T unit cell along the c-axis. Stacking vectors for the $5M_1$ and 3T mica polytypes are illustrated in Figures 10a and 10b in several different orientations. Relative layer shift of the 5-layer biotite in the HRTEM images (Figure 9) is same as stacking vectors of the 5-layer mica projected on real section corresponding to the plane containing *hhl* reciprocal spots (Figure 10).

Possible unit-cell settings for the 5-layer biotite are illustrated in Figure 11, projected onto the a–c plane of 1M mica. A supercell based on the 1M mica axial setting, with $\beta = 100°$ as measured from the SAED pattern in Figure 7a, is outlined with heavy lines. Alternatively, a supercell with $\beta = 92°$ may be chosen so

https://doi.org/10.1346/CCMN.1995.0430203 Published online by Cambridge University Press

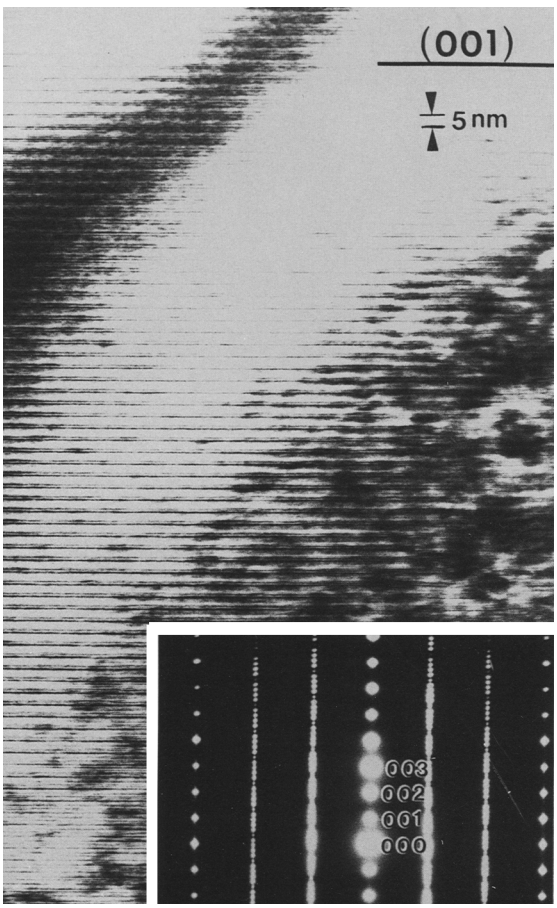

Figure 8. A dark-field image of the 5-layer biotite polytype, showing 5-nm periodicity along the c* direction. An SAED pattern of the 5-layer biotite is also inserted.

that β is near 90°. A possible space group for the 5-layer biotite polytype with the stacking sequence [02022] is *C2* (Takeda 1968, Ross, unpublished data).

There are 83 possible 5-layer polytypes involving all possible rotations (i.e., n × 60°), but only eight of these involve only 0° and ±120° rotations (Ross *et al* 1966). The stacking sequences of the other seven possible 5-layer micas are illustrated in Appendix 1. The 5-layer biotite we have observed, with the stacking sequence [02022], has been called the $5M_1$ polytype. Other reported 5-layer mica polytypes have the stacking sequences [$2\bar{2}222$], [$0002\bar{2}$], and [$22\bar{2}\bar{2}0$] (summarized by Baronnet 1992) and may be called the $5M_4$, $5Tc_1$, and $5Tc_4$ polytypes respectively (Appendices 1 and 2).

To confirm the structure of our observed 5-layer polytype, we used the computer program PTST of Takeda (1968) to calculate the periodic relative intensity distributions of diffraction spots characterizing the 5-layer mica polytypes, and the intensities for $5M_1$ biotite are given in Table 2. The intensity distribution

Table 2. Periodic intensity distribution of $5M_1$ (02022) mica.

l	02*l*	11*l*	−11*l*	20*l*
0	1.00	1.00	1.00	1.00
1	2.45	2.45	2.45	0.00
2	2.45	2.45	2.45	0.00
3	2.45	2.45	2.45	0.00
4	2.45	2.45	2.45	0.00
5	1.00	1.00	1.00	1.00

Note: 1M type axial setting with β = 100°.

in 11*l*, and 22*l* (l = 0, 1, 2, 3 . . .) is 1, 2.45, 2.45, 2.45, 2.45, 1 . . ., which corresponds to the weak•strong• strong•strong•strong•weak . . . pattern observed in the SAED pattern (Figure 7a). The calculations also indicate no additional diffraction intensity in the 20*l*, 40*l*, and 13*l* diffraction rows, as observed (Figure 7b). The $5M_1$ polytype is the only one that fits the observed intensity relationships. For comparison, the relative diffraction intensities for the other seven 5-layer micas involving 0° and ±120° rotations are listed in Appendix 2.

TEM results also show that the $5M_1$ biotite has (001) nearly parallel to (100) of the host actinolite crystal, as confirmed by an overlapped SAED pattern showing c^* of the biotite almost parallel to a^* of the actinolite (Figure 12a). A corresponding image (Figure 12b) shows $5M_1$ biotite intergrown with the actinolite. The boundaries between the two minerals exhibit more rapid beam damage than other areas because of relatively high energy along the boundaries (Figure 12b).

$1M_d$ biotite (0° and ±120° disordered rotations)

Some fine biotite grains within the primary actinolite possess disordered stacking sequences. A SAED pattern (Figure 13a) shows intense streaks in the 11*l*, and 22*l* diffraction rows, with intensity maxima at the 1M mica diffraction positions. A dark-field image formed from the 110 diffraction spot shows a high density of stacking faults in the crystal, which may be described as highly faulted 1M biotite. A HRTEM image of the disordered biotite shows the relative layer shifts and indicates that the crystal is composed primarily of 1M and $2M_1$ biotite domains with stacking faults (Figure 13c). The area indicated by a large arrow shows unusually rapid radiation damage, which possibly was induced by relatively lower K occupancies in the interlayer sites. Diffraction patterns show streaking only in *hkl* ($k \neq 3n$) diffraction rows, indicating that the stacking disorder in the biotite involves only 0° and ±120° rotations (Ross *et al* 1966). This stacking-disordered biotite has (001) parallel to (100) of the actinolite (Figure 14). The (010) boundary between actinolite and $1M_d$ biotite in this figure appears to be coherent.

https://doi.org/10.1346/CCMN.1995.0430203 Published online by Cambridge University Press

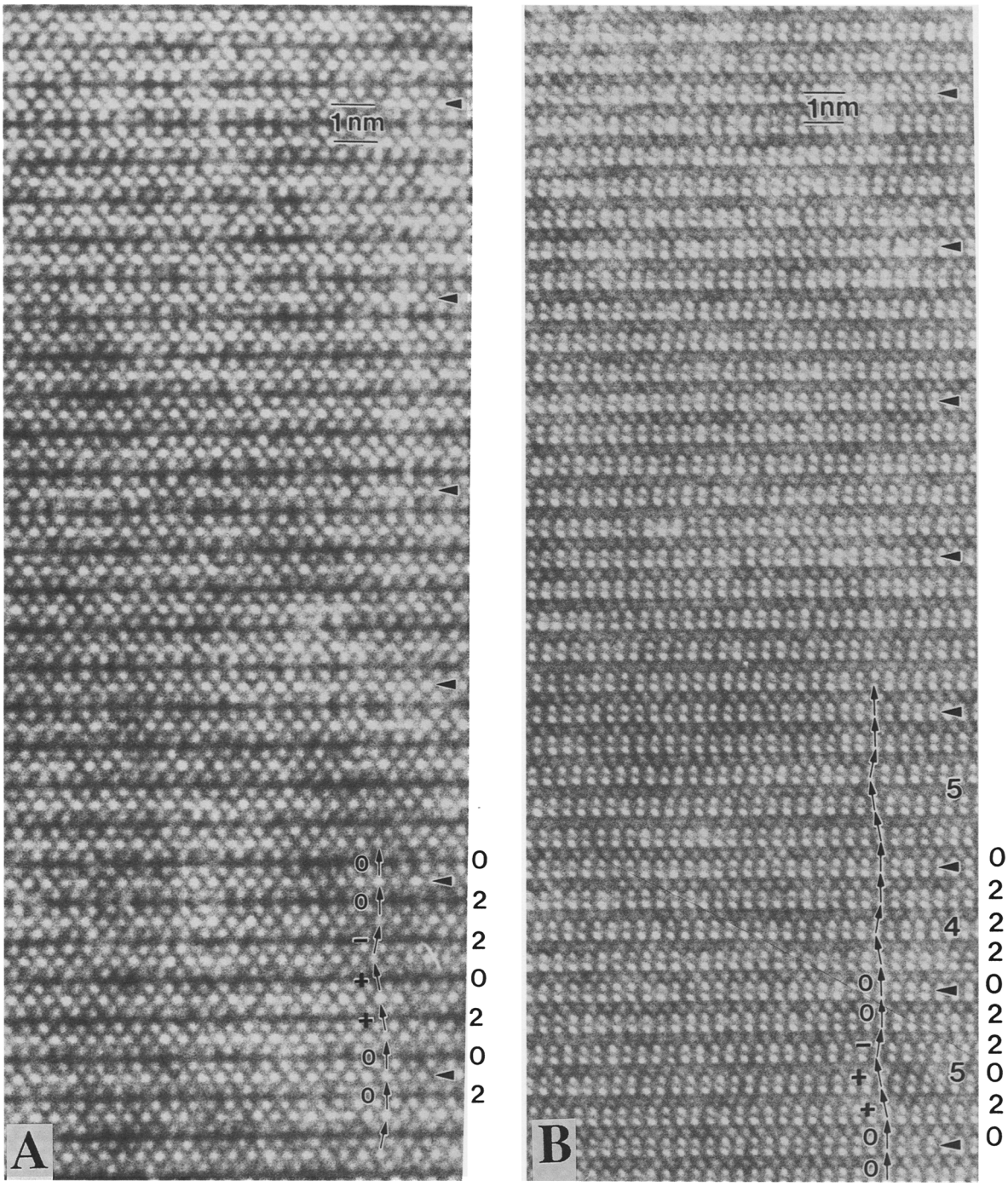

Figure 9. (A) HRTEM image of the 5-layer biotite polytype at a defocus value of about −750 Å, showing a periodic shift after every five layers. The stacking sequence indicated by the layer shift is [02022]. (B) HRTEM image of the 5-layer biotite polytype at a defocus value of about −1250 Å, showing a periodic shift after every five layers (labeled 5) with the stacking sequence [02022]. An area with a 4-layer sequence (labeled 4) shows the stacking sequence [0222], corresponding to the stacking of one unit cell of the 1M polytype and one unit of cell of the 3T polytype.

https://doi.org/10.1346/CCMN.1995.0430203 Published online by Cambridge University Press

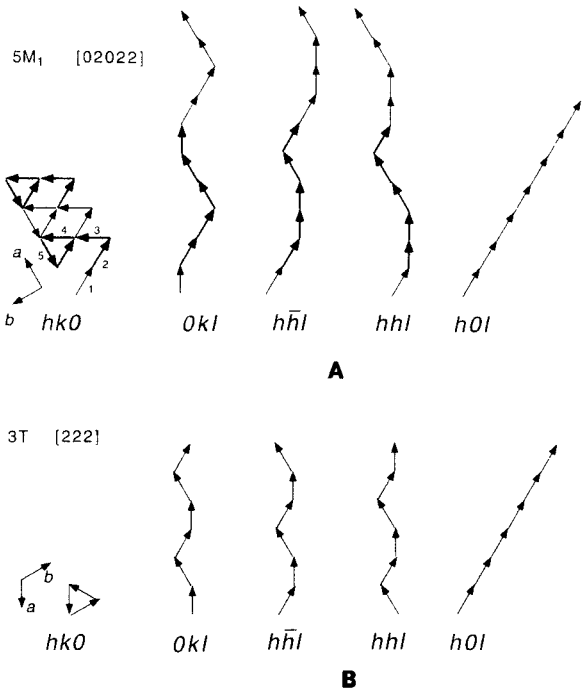

Figure 10. Diagrams showing stacking vectors for the 5-layer biotite (A), and 3T biotite (B) polytypes in different real-space sections.

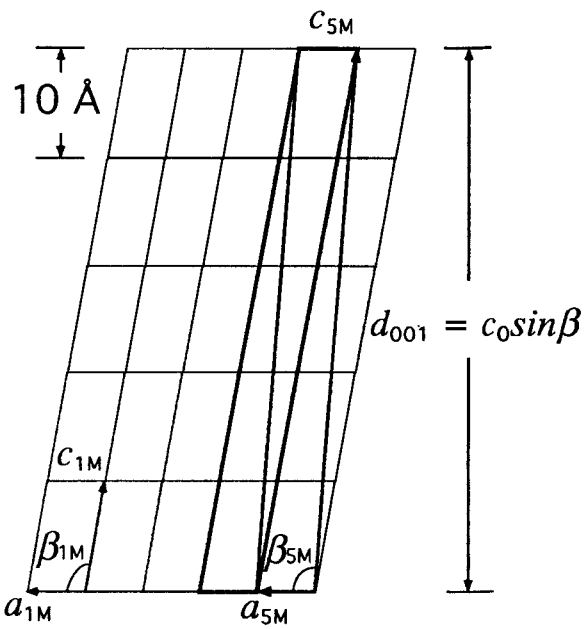

Figure 11. Diagram showing relationships between the 1M polytype orientation (β = 100°) and a $5M_1$ polytype orientation on the a–c plane (bold lines). An alternative supercell with β = 92° for the $5M_1$ polytype is outlined.

$1M_d$ biotite ($\pm n \times 60°$ disordered rotations)

As noted before, the most common stacking faults in disordered biotite involve 0° and ±120° rotations. However, some areas of the biotite also show streaking in *hkl* ($h \neq 3n$) diffraction rows (Figure 15b), indicating that the stacking faults in this area involve rotations of the type $\pm n \times 60°$ (Ross *et al* 1966). A one-dimensional HRTEM image (Figure 15a) shows domains from such an area with periodicities of 1 nm, 2 nm, 3 nm, and 4 nm. Interpretation of stacking sequences in such areas is complex, due to ambiguity in projected stacking vectors in HRTEM images. Domains with 2-nm periodicity on this orientation could be either the $2M_2$ or 2Or polytype, and those with 1-nm periodicity could be either the 1M or $2M_1$ structure. Interpretation for domains with 3-nm and 4-nm periodicities is even more complex. Such $\pm n \times 60°$ stacking disorder is not common in trioctahedral micas (Ross *et al* 1966).

AEM results from the biotite polytypes

Structural formulae of biotite were calculated based on 11 oxygenes. Fe was assumed to be ferrous and in octehedral sites together with Mg. Structural formulae of 1M, $5M_1$, and stacking-disordered ($1M_d$) biotite from AEM analyses are listed in Table 1. The $1M_d$ biotite is lower in Ti and K than the other polytypes (Table 1, Figure 16). The bonding force between neighboring 2:1 layers of the $1M_d$ biotite may be relatively weak because of low occupancies of K in the interlayer positions. It can be inferred that stacking disordering in the low-K biotite will be more easily induced by external factors such as fluctuation of fluid composition. There also appears to be a small difference in Ti between the 1M and $5M_1$ biotite (Figure 16). The biotite compositions from AEM are similar to those previously reported for biotite formed during propylitic alteration (see Table 1 of Bowman *et al* 1987). Thus, it is likely that all of the biotite crystals within primary actinolite formed during propylitic alteration of the monzonite.

DISCUSSION

Reaction from actinolite to biotite

The temperature for the alteration reactions in this specimen was estimated at about 450°C (Bowman *et al* 1987). Based on orientation relationship between actinolite and biotite, the reaction from actinolite to biotite may involve dissolution of the actinolite and crystallization of biotite on the amphibole matrix. Presumably, the nucleation of biotite is heterogeneous, and compositional change was achieved by transport via hydrothermal solution. Potassium and aluminum for the biotite formation could be from dissolution of K-feldspars during the alteration. The reaction from actinolite to biotite may be approximated as

https://doi.org/10.1346/CCMN.1995.0430203 Published online by Cambridge University Press

$$\underset{\text{Actinolite}}{Ca_2(Mg,Fe)_5[Si_8O_{22}](OH)_2} + 2KAlSi_3O_8 + Mg^{2+} + 2H^+ \rightarrow \underset{\text{Biotite}}{2K(Mg,Fe)_3[Si_3AlO_{10}](OH)_2} + 2Ca^{2+} + \underset{\text{Quartz}}{8SiO_2}.$$

It can be known from the above reaction that fluid properties (e.g., activities of Mg^{2+}, Ca^{2+} and H^+) also affect the reaction from actinolite to biotite. Hydrothermal fluid with high Mg^{2+} activity favors the biotite formation. Fluctuation of the fluid composition may affect the reaction rate and stacking structure of biotite layers during crystallization.

The genesis of nonperiodic stacking in biotite

Nonperiodic (or disordered) layer stacking in biotite can be induced by deformation of an ordered crystal because the bonding between neighboring layers is relatively weak. For instance, stacking faults in some phyllosilicate minerals can be introduced by grinding. In the present occurrence, however, the disordered stacking of $1M_d$ biotite crystals coexisting with ordered 1M and $5M_1$ biotite crystals apparently was not induced by external stress because there is no obvious deformation of the host actinolite or ordered biotite crystals. Thus, the disordered $1M_d$ biotite is probably formed during crystallization from the hydrothermal fluid.

There are several models or theories proposed for the growth of ordered mica polytypes (see review by Baronnet 1992). However, only one model has been proposed for the growth of nonperiodic polytypes and the intergrowth of different ordered polytypes and disordered structure far from the equilibrium state (Vignoles 1992). The model proposed by Vignoles (1992) for SiC crystallization is based on the fine structure (or local structural deformation) of unit layers in different ordered polytypes and possible structural deformation during deposition of a new SiC layer at two possible positions. Vignoles (1992) proposed a qualitative logistic map (actually a circle map: Hao 1984, Baker and Gollub 1990) for SiC crystals to account for long-period SiC polytypes, nonperiodic (chaotic) stacking, and intergrowth of different polytypes. Here we propose an alternative dynamical model for the formation of non-

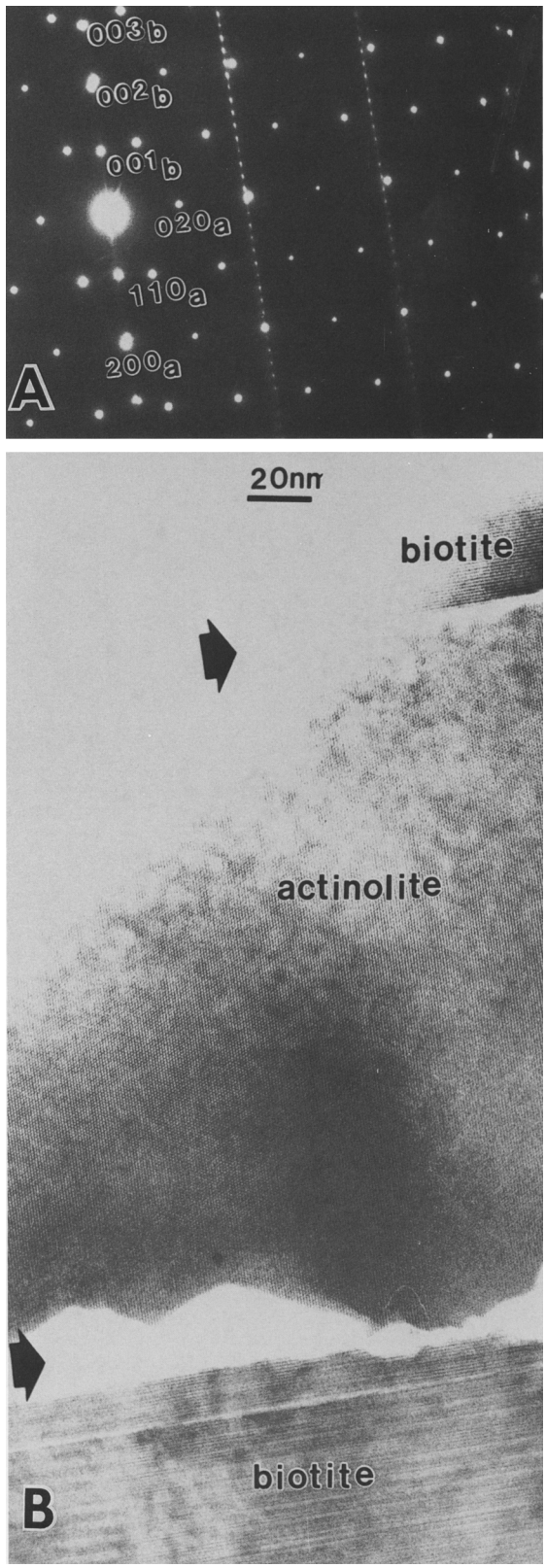

Figure 12. (a) SAED pattern from overlapping 5-layer biotite and its neighboring actinolite, showing that the a^* direction of actinolite is close to c^* of the biotite. (b) A corresponding HRTEM image showing boundaries (large arrows) between the 5-layer biotite polytype and actinolite.

https://doi.org/10.1346/CCMN.1995.0430203 Published online by Cambridge University Press

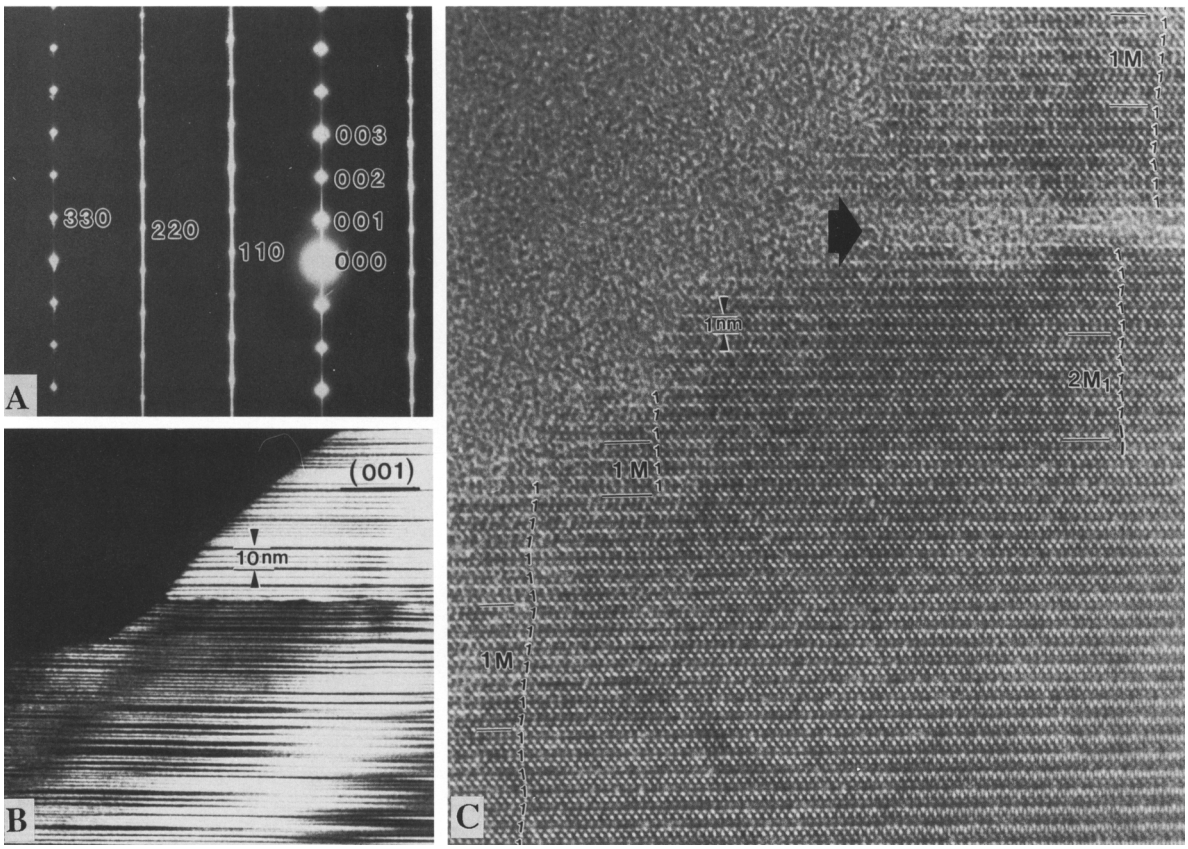

Figure 13. (a) SEAD pattern from disordered biotite showing strong streaking in the 11*l* and 22*l* diffraction rows. (b) A dark-field image showing a high density of stacking faults within the biotite. (c) HRTEM image of the $1M_d$ biotite, showing stacking faults and thin domains with 1M and $2M_1$ structure.

periodic stacking sequences formed under non-equilibrium state which could be caused by compositional fluctuation of fluid during crystallization. No attempt will be made to discuss the energetics of ordered polytypes.

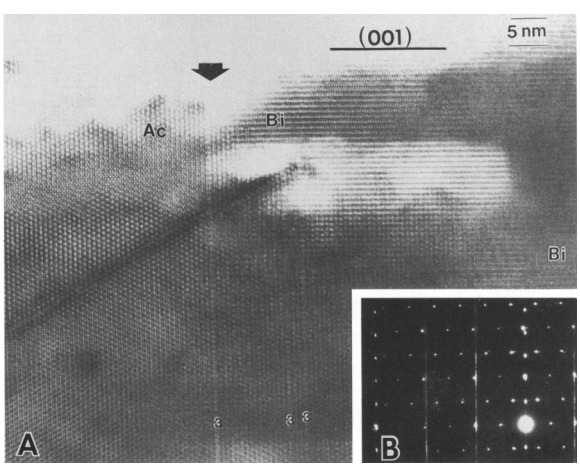

Figure 14. HRTEM image (A) and SAED pattern (B), showing the orientation relationship and an overlapped boundary between $1M_d$ biotite (Bi) and actinolite (Act). Triple chains are labeled "3."

Although the structural difference between 1M and $2M_1$ muscovite polytypes is very obvious (Bailey 1984), structural information on different biotite polytypes with the same composition is very limited. The only clear data are from coexisting 1M and $2M_1$ biotite polytypes with identical composition and unit-cell parameters (Takeda and Ross 1975). The largest structural difference between them is displacement of the O3 and O4 oxygen atoms along the $\pm b$ directions in the $2M_1$ polytype. This displacement reduces the symmetry of the $2M_1$ unit layer to $C\bar{1}$, rather than $C2/m$ as in the 1M polytype (Takeda and Ross 1975). It is possible that the structure of unit layers in the 3T polytype is different from those of the 1M and $2M_1$ polytypes, but there are no similar data for this case. Here we assume that 2:1 layers of the 1M, $2M_1$, and 3T

https://doi.org/10.1346/CCMN.1995.0430203 Published online by Cambridge University Press

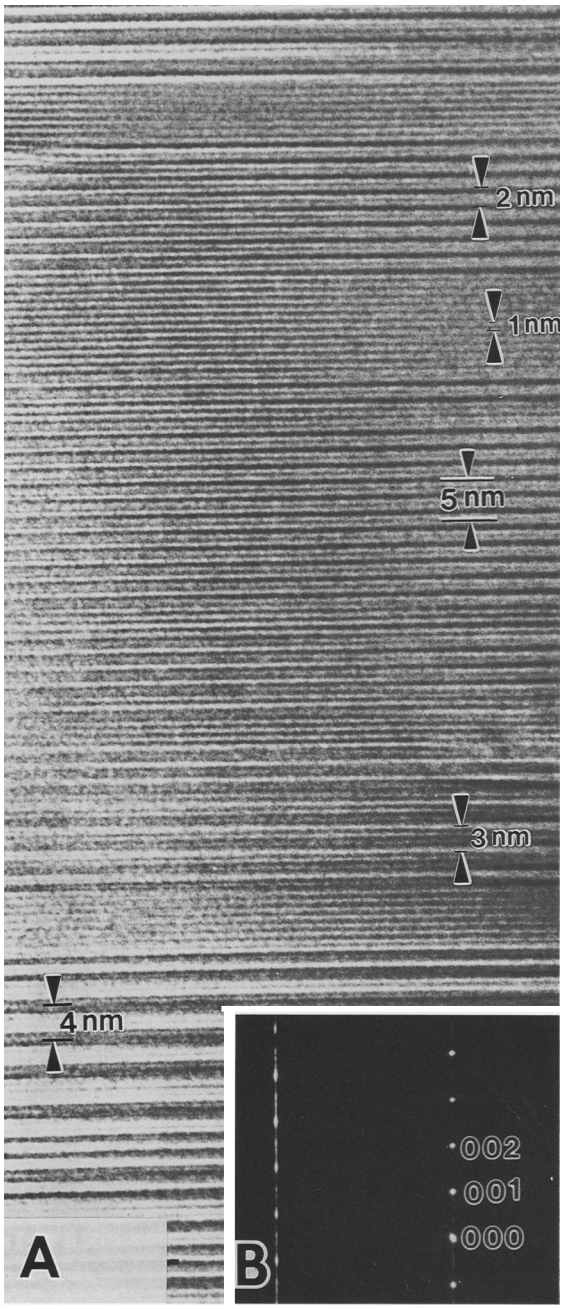

Figure 15. (a) HRTEM image from an area with n × 60° rotational disorder, showing layer dominans with 1-nm, 2-nm, 3-nm, and 4-nm periodicities. (b) SAED pattern from this area showing streaking of the 13l (i.e., hkl, h ≠ 3n) diffraction row caused by n × 60° rotational disorder.

biotite polytypes are all structurally distinct in some way.

In nature, the most common polytype for biotite is 1M, and $2M_1$ and 3T being less common. Assuming that 1M is the most stable structure for biotite and that

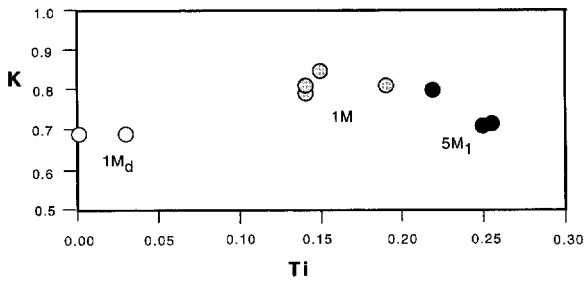

Figure 16. A diagram showing the relationship between K and Ti contents of 1M, $1M_d$, and $5M_1$ biotite crystals.

$2M_1$ and 3T are less stable, the chemical potential relating these structures may be like the one schematically illustrated in Figure 17. The potential is periodic with respect to atomic displacements and symmetry of the 2:1 layers along a coordinate of structural states. The relative energies of the potential wells for the 1M, $2M_1$, and 3T structures may change as functions of temperature, pressure, and crystal composition. For instance, the most stable structure for muscovite under many geological conditions is probably $2M_1$, since $2M_1$ muscovite is the most abundant polytype in nature. Chemical potentials for the different structures also influence the formation probabilities for their nuclei.

During the crystallization of biotite from either a magma or hydrothermal solution, the ideally crystallized structure at equilibrium will be the 1M polytype because of its low energy minimum, according to Figure 17. The $2M_1$ and 3T polytypes, with higher potential minima, can also crystallize metastably. If an external force arising from compositional fluctuation of fluid affects the crystallization of biotite, the complex (dynamical) interaction between the growing crystal and the external force may induce complex (nonperoidic or chaotic) structural oscillations among the three structural states (i.e., 1M, $2M_1$, and 3T). According to the schematic potential of Figure 17, structural oscillation between 1M and $2M_1$ structures is relatively easy because of relatively low energy barrier between them. Nonperiodic oscillation corresponds to the intergrowth of 1M, and $2M_1$ polytype domains such as in observed $1M_d$ biotite (Figure 13), as well as intergrowth of ordered (periodic) and disordered (nonperiodic) polytypes.

Under some special conditions, periodic oscillations may occur, corresponding to periodic intergrowth of 1M, $2M_1$, and/or 3T structural layers (or domains). Some reported long-period biotite polytypes could result from such periodic oscillation, although spiral growth resulting from screw dislocations probably is responsible for many such structures. For periodic oscillations between the 1M and $2M_1$ structures, the 1M and 3T structures, or the $2M_1$ and 3T structures, it is possible to form long-period polytypes with the stack-

https://doi.org/10.1346/CCMN.1995.0430203 Published online by Cambridge University Press

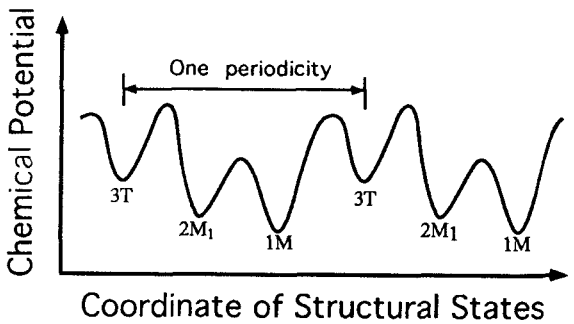

Figure 17. Schematic diagram of chemical potential versus a coordinate of structural state for a system with 1M, $2M_1$, and 3T polytype structures. The potential is assumed to be periodic with respect to a structural parameter, e.g., atomic displacement within the unit layers, so that structural oscillation between structural states can occur.

ing sequences $[(0)_m(22)_n]$, $[(0)_m(222)_p]$, or $[(22)_n(222)_p]$ respectively, where m, n, and p are non-negative integers. If periodic oscillation occurs among the 1M, $2M_1$, and 3T structural states, complex long-period polytypes with stacking sequences of $[(0)_m(22)_n(222)_p)]$ or even more complicated sequences may occur.

In principle, the proposed dynamical model could account for any ordered mica polytype, any disordered stacking sequence in a mica, or any intergrowth involving different polytypes. Similarly, previous models based on either equilibrium or kinetic theories (e.g., spiral growth) can also be used to explain such phenomena involving complex mica polytypes and polytype intergrowths (Baronnet 1992). The proposed model involving structural oscillation may be applicable to some occurrences of micas forming during crystallization under non-equilibrium state due to compositional fluctuation of fluids. It is easier to induce stacking disorder in low-K mica because of relatively weak force between neighboring 2:1 layers with respect to external force arising from compositional fluctuation of fluid. Nonperiodic oscillations (or stacking) in biotite formed via this process will be chaotic (that is, a deterministic structure), rather than random. Using nonlinear dynamics, it would be possible to obtain numerical solutions for non-equilibrium biotite growth if a reasonable chemical potential relating the structural difference among the 1M, $2M_1$, and 3T polytypes could be developed.

CONCLUSIONS

Primary actinolite in quartz monzonite from the Bingham Canyon, Utah, porphyry copper deposit contains small inclusions of biotite and smectite which apparently formed during propylitic and argillic alteration respectively. The layer silicates probably grew by a dissolution/crystallization mechanism with heterogeneous nucleation occurring on the actinolite structure.

The most abundant polytype in the biotite is 1M, and the most common type of stacking fault is a layer with $-120°$ rotation followed by a layer with $+120°$ rotation which corresponds to one unit cell of $2M_1$ polytype inserted into the 1M structure. Stacking-disordered ($1M_d$) biotite also occurs, and it may be considered as a nonperiodic intergrowth of 1M and $2M_1$ polytype domains with stacking faults along the *c*-axis. A new 5-layer polytype was observed, and its structure was determined by SAED and HRTEM methods to be the $5M_1$ structure with the stacking sequence [02022].

A qualitative model of structural oscillation among the 1M, $2M_1$, and 3T structural states is proposed as one possible mechanism for forming nonperiodic stacking sequences during biotite crystallization. Nonperiodic stacking in biotite formed in this way should consist of nonperiodic intergrowths of different structural layers or intergrowths of larger domains with the 1M, $2M_1$, and 3T structures. The model also explains complex, long-period polytypes and the intergrowth of ordered and disordered polytypes formed during non-equilibrium crystallization.

ACKNOWLEDGMENTS

We thank J. R. Bowman for supplying the sample used in this study, E. S. Ilton for valuable discussions on the occurrence of biotite in porphyry copper deposits, Michael O'Keefe for allowing us to use a demonstration version of the MACTEMPAS computer program, Mac Ross and Alain Baronnet for discussing on long-period mica polytypes, H. Takeda for providing a computer program calculating periodic intensity distributions of mica polytypes, and S. Tsipursky for helpful comments on the manuscript. This work was supported by DOE grant DE-FG02-89ER14074 and NSF grant EAR89-03630. Electron microscopy was performed in the HRTEM/AEM laboratory at Johns Hopkins, which was established with partial support from NSF grant EAR8300365.

REFERENCES

Amouric, M., G. Mercuriot, and A. Baronnet. 1981. On computed and observed HRTEM images of perfect mica polytypes. *Bulletin de Minéralogie* **104**: 298–313.

Amouric, M., and A. Baronnet. 1983. Effect of early nucleation conditions on synthetic muscovite polytypism as seen by high resolution transmission electron microscopy. *Physics and Chemistry of Minerals* **9**: 146–159.

Bailey, S. W., V. A. Frank-Kamenetskii, S. Goldstaub, A. Kato, A. Pabst, H. Schultz, H. F. W. Taylor, M. Fleisher, and A. J. C. Wilson. 1977. Report of the IMA-IUCr joint committee on nomenclature. *Acta Crystall.* **A33**: 681–684.

Bailey, S. W. 1984. Crystal chemistry of the true micas. In *"Micas," Reviews in Mineralogy*. S. W. Bailey, ed. Washington, D.C.: Mineral Society of America, **Vol 13**: 13–60.

Bailey, S. W. 1988. X-ray identification of the polytypes of mica, serpentine, and chlorite. *Clays & Clay Miner.* **36**: 193–213.

Baker, G. L., and J. P. Gollub. 1990. *Chaotic Dynamics:*

An Introduction. Cambridge: Cambridge University Press, 182 pp.

Baronnet, A. 1975. Growth spirals and complex polytypism in micas. I. Polytypic structure generation. *Acta Crystallog.* **A31**: 345–355.

Baronnet, A. 1982. Ostwald ripening in solution, the case of calcite and mica. *Estudios Geologicos* **38**: 185–198.

Baronnet, A., and Z. C. Kang. 1989. About the origin of mica polytypes. *Phase Transitions* **16/17**: 477–493.

Baronnet, A. 1992. Polytypism and stacking disorder. In "*Minerals and Reactions at the Atomic Scale: Transmission Electron Microscopy,*" P. R. Buseck, ed. *Reviews in Mineralogy.* Washington, D.C.: Mineral Society of America, Vol. 22, 231–288.

Bowman, J. R., W. T. Parry, W. P. Kropp, and S. A. Kruer. 1987. Chemical and isotopic evolution of hydrothermal solutions at Bingham Utah. *Econ. Geol.* **82**: 395–428.

Gjonnes, J., and A. F. Moodie. 1965. Extinction conditions in the dynamic theory of electron diffraction. *Acta Crystallog.* **19**: 65–67.

Hao, B.-L. 1984. *Chaos.* Singapore: World Scientific, 576 pp.

Hazen, R. M., and C. W. Burnham. 1973. The crystal structures of one-layer phlogopite and annite. *Amer. Miner. q ww***58**: 889–900.

Iijima, S., and P. R. Buseck. 1978. Experimental study of disordered mica structures by high-resolution electron microscopy. *Acta Crystallog.* **A34**: 709–719.

Livi, K. J. T., and D. R. Veblen 1987. "Eastonite" from Easton, Pennsylvania: A mixture of phlogopite and a new form of serpentine. *Amer. Miner.* **72**: 113–125.

Ross, M., M. Takeda, and D. R. Wones. 1966. Mica polytypism: Description and identification. *Science* **151**: 191–193.

Smith, J. V., and H. S. Yoder, Jr. 1956. Experimental and theoretical studies of the mica polymorphs. *Mineral. Mag.* **69**: 252–263.

Takeda, H. 1968. PTST (a FORTRAN program calculating periodic intensity distributions of mica polytypes). Personal communication, 1991.

Takeda, H., and M. Ross. 1975. Mica polytypism: Dissimilarities in the crystal structures of coexisting 1M and $2M_1$ biotite. *Amer. Miner.* **60**: 1030–1040.

Vand, V., and J. I. Hanoka. 1967. Epitaxial theory of polytypism. Observations of the growth of PbI_2 crystals. *Materials Research Bulletin* **2**: 241–251.

Veblen, D. R. 1981. Non-classical pyriboles and polysomatic reactions in biopyriboles. In "*Amphiboles and Other Pyriboles—Mineralogy,*" D. R. Veblen, ed. *Reviews in Mineralogy,* vol. **9A**: 189–236, Washington, D.C.: MSA.

Veblen, D. R. 1985. Direct TEM imaging of complex structures and defects in silicates. *Annual Review of Earth and Planetary Sciences* **13**: 119–146.

Veblen, D. R., and D. L. Bish. 1988. TEM and X-ray study of orthopyroxene megacrysts: Microstructures and crystal chemistry. *Amer. Miner.* **73**: 677–691.

Verma, A. R., and P. Krishna. 1966. *Polymorphism and Polytypism in Crystals.* Wiley, New York, 83 pp.

Vignoles, G. L. 1992. Atomic relaxation and dynamical generation of ordered and disordered CVI SiC polytypes. *J. Crystal Growth* **118**: 430–438.

(Received 8 February 1994; accepted 23 August 1994; Ms. 2466)

APPENDIX

Appendix 1. Stacking vectors in other 5-layer mica polytypes involving only 0° and ±120°.

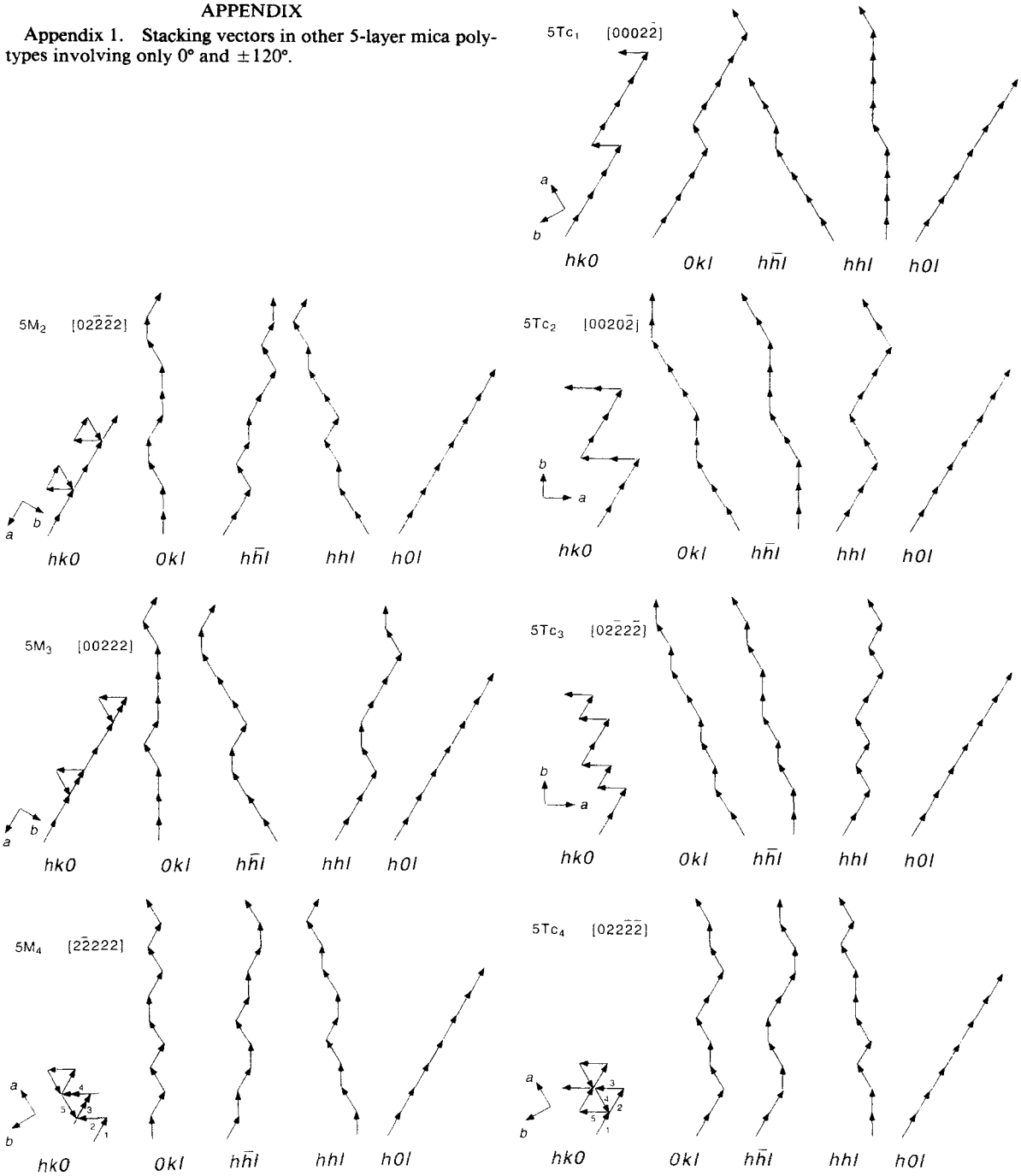

https://doi.org/10.1346/CCMN.1995.0430203 Published online by Cambridge University Press

Appendix 2. Periodic intensity distributions in other 5-layer mica polytypes involving only 0° and ±120°.

$5M_2$ ($02\bar{2}\bar{2}2$) mica

l	*02l*	*11l*	*-11l*	*20l*
0	2.65	2.65	2.65	5.00
1	2.80	2.80	2.80	0.00
2	1.07	1.07	1.07	0.00
3	1.07	1.07	1.07	0.00
4	2.80	2.80	2.80	0.00
5	2.65	2.65	2.65	5.00

$5M_3$ (00222) mica

l	*02l*	*11l*	*-11l*	*20l*
0	3.61	3.61	3.61	5.00
1	1.73	1.73	1.73	0.00
2	1.73	1.73	1.73	0.00
3	1.73	1.73	1.73	0.00
4	1.73	1.73	1.73	0.00
5	3.61	3.61	3.61	5.00

$5M_4$ ($2\bar{2}222$) mica

l	*02l*	*11l*	*-11l*	*20l*
0	2.65	2.65	2.65	5.00
1	1.07	1.07	1.07	0.00
2	2.80	2.80	2.80	0.00
3	2.80	2.80	2.80	0.00
4	1.07	1.07	1.07	0.00
5	2.65	2.65	2.65	5.00

Note: 1M type axial setting with β=100°.

$5Tc_1$ (00022) mica

l	*02l*	*11l*	*-11l*	*20l*
0	1.00	1.00	1.00	5.00
1	2.13	0.87	0.87	0.00
2	4.17	1.17	1.17	0.00
3	1.17	4.17	4.17	0.00
4	0.87	2.13	2.13	0.00
5	1.00	1.00	1.00	5.00

$5Tc_2$ ($00\bar{2}02$) mica

l	*02l*	*11l*	*-11l*	*20l*
0	2.00	2.00	2.00	5.00
1	1.41	3.45	3.45	0.00
2	0.72	2.57	2.57	0.00
3	2.57	0.72	0.72	0.00
4	3.45	1.41	1.41	0.00
5	2.00	2.00	2.00	5.00

$5Tc_3$ ($02\bar{2}2\bar{2}$) mica

l	*02l*	*11l*	*-11l*	*20l*
0	1.00	1.00	1.00	5.00
1	1.17	4.17	4.17	0.00
2	2.13	0.87	0.87	0.00
3	0.87	2.13	2.13	0.00
4	4.17	1.17	1.17	0.00
5	1.00	1.00	1.00	5.00

$5Tc_4$ ($02\bar{2}\bar{2}2$) mica

l	*02l*	*11l*	*-11l*	*20l*
0	2.00	2.00	2.00	5.00
1	0.72	2.57	2.57	0.00
2	3.45	1.41	1.41	0.00
3	1.41	3.45	3.45	0.00
4	2.57	0.72	0.72	0.00
5	2.00	2.00	2.00	5.00

https://doi.org/10.1346/CCMN.1995.0430203 Published online by Cambridge University Press